ELSEVIER

Journal of Alloys and Compounds 217 (1995) 5–12

Journal of ALLOYS AND COMPOUNDS

Solid state chemistry of Nb_3Cl_8: Nb_3TeCl_7, mixed crystal formation, and intercalation

Gordon J. Miller

Department of Chemistry, Iowa State University, Ames, IA 50011, USA

Received 5 April 1994; in final form 7 June 1994

Abstract

The layered niobium cluster halide, α-Nb_3Cl_8, offers a potentially rich chemistry because of its morphology and electronic structure. Substitution of chloride by telluride, driving forces for mixed crystal formation, and possible structural distortions on intercalation in α-Nb_3Cl_8 are probed using both experimental and theoretical techniques. The compound Nb_3TeCl_7 has been synthesized in quantitative yield from the reactants Nb, $NbCl_5$, and Te and has been structurally characterized by single-crystal X-ray diffraction. Nb_3TeCl_7 crystallizes in the space group $P\bar{3}m1$ (no. 164); $a = 6.8985(12)$ Å; $c = 12.6351(26)$ Å; $Z = 2$; $R = 0.0238$; $wR = 0.0392$. The structure consists of Nb_3 triangular clusters singly capped by μ_3-Te atoms. Physical measurements and semiempirical electronic structure calculations demonstrate the closed subshell nature of the bonding in this compound. In addition, these calculations predict a structural instability for Nb_3Cl_8-type halides when the cluster valence electron concentration rises above 7.5 electrons per Nb_3 cluster, and provide a rationale for the observed homogeneity width within the α-$Nb_{3-x}Cl_8$ system ($0 \leqslant x \leqslant 0.5$).

Keywords: Solid state chemistry; Niobium cluster halides; Mixed crystal formation

1. Introduction

The nature of transition metal–chalcogenide interactions is governed primarily by the degree of charge transfer that occurs from the metal to the more electronegative chalcogen atom [1]. As is clear from the trend in structures observed for the transition metal dichalcogenides, the more electronegative metals on the right-hand side of the transition series, e.g. Fe, Co, Ru, Pt, show just a partial reduction of the chalcogen to give dichalcogenide dianions, i.e. S_2^{2-}, Se_2^{2-}, and Te_2^{2-} [2]. Since electronegativity increases with increasing oxidation state of the metal, the early transition metals in high oxidation states also show dichalcogenide dianions, as in TiS_3 [3] and NbS_3 [4].

Tellurium, the most electropositive of the chalcogens (aside from polonium, of course), shows exceptional behavior with nearly all transition metals, and this has been attributed to just a partial charge transfer from the metal to tellurium [5]. Unusually low c/a ratios for CdI_2-type metal ditellurides represent just one of numerous structural features for these systems that can be rationalized by this argument of "internal redox competition" [1,6].

As part of a research program designed to probe this type of interaction in the solid state, we have pursued substitutional derivatives of reduced niobium halides in order to assess the relative energetics of Nb and Te. The halide matrix offers the ability to tune the oxidation state of Nb and, thus, to dictate the degree of charge transfer from Nb to Te. In this article we report the synthesis, structure, properties, and electronic structure of a new compound in the Nb–Te–Cl system: Nb_3TeCl_7. During the course of these investigations, we have also expanded our understanding of the system α-Nb_3Cl_8 and report on our theoretical investigations that elucidate electronic driving forces for the observed homogeneity width in this system, as well as potential electronic instabilities that may lead to local structural distortions on intercalation by alkali metals.

2. Experimental details

2.1. Synthesis

Nb_3TeCl_7 was synthesized in quantitative yield by heating a stoichiometric mixture of $NbCl_5$ powder (ALFA, twice sublimed in a Pyrex Schlenk tube to remove $NbOCl_3$), Nb turnings (ALFA, cleaned with HF–HNO_3, and dried under high vacuum at 1370 K

SSDI 0925-8388(94)01298-V

for 12 h), and Te powder (ALFA, used as supplied), in a quartz ampoule (7 cm long, 1.5 cm in outer diameter) to 1090 K with a minimal temperature gradient for one week. This temperature was selected after observing a small endothermic effect near 1070 K for the same stoichiometric mixture of $NbCl_5$, Nb, and Te using differential thermal calorimetry (Netsch). At that time, the ampoules were either quenched or slowly cooled (ca. 1 K min^{-1}) to room temperature, and the product was handled exclusively in an Ar-filled glove-box. The product is stable in air, and decomposes slowly in water. Electron probe microanalysis using an ARL SEMQ microprobe confirmed the presence of Nb, Te, and Cl in the homogeneous sample.

2.2. Structure determination

The product gives thin black plates with typical dimensions less than 0.3 mm. Crystals were selected and checked using Weissenberg techniques. Crystals suitable for single-crystal X-ray structure determination were isolated only from the rapidly quenched samples. All crystals from the slowly cooled preparations showed evidence for twinning. Nevertheless, X-ray powder diffraction patterns, taken on an Enraf–Nonius Guinier camera using monochromatized Cu $K\alpha_1$ radiation, for both samples identified the α-Nb_3Cl_8 structure type [6] as the only phase present. With silicon powder as an internal standard, the Guinier pattern of Nb_3TeCl_7 was successfully indexed with a hexagonal unit cell ($a = 6.8985(12)$ Å, $c = 12.6351(26)$ Å) using 30 reflections in the 2θ range between 29° and 85°.

A crystal with dimensions 0.12 mm × 0.15 mm × 0.05 mm was placed in an Ar-filled capillary and mounted on an Enraf–Nonius CAD4 diffractometer. Unit cell parameters were determined by least-squares analysis of 24 centered reflections with $20° \leqslant 2\theta \leqslant 35°$ ($a = 6.880(2)$ Å, $c = 12.609(3)$ Å). Further relevant crystallographic data are summarized in Table 1.

The data indicated a Laue class of $\bar{3}m1$, and we selected α-Nb_3Cl_8 which adopts the space group $P\bar{3}m1$ with no systematic absences, as a model from which to solve the structure [6]. The refinement utilized 494 independent, observed reflections ($F_o \geqslant 4\sigma(F_o)$) for 26 parameters, and yielded the residuals $R = 0.0238$, $wR = 0.0392$, with a goodness of fit of 1.08 (SHELXTL-PLUS) [7]. The difference Fourier map did not show any additional significant chemical features. Furthermore, comparison between the calculated and observed X-ray powder patterns showed excellent agreement of intensities, with the largest deviation of a 2θ value of 0.08°. Table 2 lists the positional and displacement parameters and Table 3 contains some selected bond lengths and bond angles for Nb_3TeCl_7. Atomic scattering factors and anomalous dispersion corrections were taken from the *International Tables for X-Ray Crystallography* [8]. (A complete listing of all crystallographic data, both from single-crystal and powder diffraction measurements, may be obtained from the author).

Table 1
Structure determination summary for Nb_3TeCl_7

Space group	$P\bar{3}m1$ (No. 164)
Unit cell dimensions	$a = 6.8985(12)$ Å
	$c = 12.6351(26)$ Å
Volume	520.73(15) Å^3
Z	2
Density (calculated)	4.205 Mg m^{-3}
Crystal size (mm^3)	0.12 × 0.15 × 0.05
Absorption coefficient	7.776 mm^{-1}
Radiation	Mo Kα ($\lambda = 0.710\,73$ Å)
Temperature (K)	295(1)
2θ range	3.0–55.0°
Scan range (ω)	1.50°
Scan speed	Variable; 1.64°–5.47° min^{-1} in ω
Index ranges	$0 \leqslant h \leqslant 7$, $0 \leqslant k \leqslant 7$,
	$-16 \leqslant l \leqslant 16$
Reflections collected	977
Independent reflections	498 ($R_{int} = 0.028$)
Observed reflections	494 ($F_o \geqslant 4\sigma(F_o)$)
Minimum, maximum transmission	0.444, 0.0973
Extinction correction	0.0013(2)
Weighting scheme	$w = 1/[\sigma^2(F_o^2) + 0.0116P)^2]$
	where $P = (F_o^2 + 2F_c^2)/3$
Parameters refined	26
R indices ($F_o \geqslant 4\sigma(F_o)$)	$R = 0.0238$, $wR = 0.0392$
R indices (all data)	$R = 0.0254$, $wR_2 = 0.0409$
Goodness of fit, all data	1.08
Data-to-parameter ratio	19.0:1
Largest difference peak	1.06 e Å^3
Largest difference hole	−1.35 e Å^3

Table 2
Positional coordinates and equivalent isotropic displacement coefficients for Nb_3TeCl_7 (all site occupation factors are 1.0)

Atom	Site	x	y	z	U_{eq}
Nb	6i	0.5262(1)	−0.5262(1)	0.7597(1)	0.008(1)
Te	2d	2/3	1/3	0.5918(1)	0.011(1)
Cl(1)	2d	1/3	2/3	0.8677(2)	0.012(1)
Cl(2)	6i	0.8322(1)	−0.8322(1)	0.8838(1)	0.013(1)
Cl(3)	6i	0.1658(1)	−0.1658(1)	0.6581(1)	0.013(1)

Table 3
Selected bond distances (ängströms) and angles (degrees) in Nb_3TeCl_7

Nb–Nb	2.898(1), 3×	Nb–Nb–Nb	60.0(1), 3×
Nb–Te	2.700(1), 3×	Nb–Cl1	2.672(1), 3×
Nb–Cl2	2.416(1), 6×	Nb–Cl3	2.515(1), 6×
Nb–Te–Nb	64.9(1), 3×	Nb–Cl1–Nb	96.3(1), 3×
Nb–Cl2–Nb	73.7(1), 3×	Nb–Cl3–Nb	104,7(1), 6×

2.3. Physical measurements

The magnetic susceptibility of Nb_3TeCl_7 was measured using a Quantum Designs superconducting quantum interference device magnetometer operated at 2 T between 4 and 350 K. After adjusting the data for a diamagnetic core correction [9], Nb_3TeCl_7 shows temperature-independent diamagnetism, which suggests a closed-shell electronic configuration. Two-probe electrical resistivity measurements indicated $\rho(295\ K) \approx 10^3$ Ω cm.

2.4. Theoretical calculations

Electronic structure calculations utilized the extended Hückel ansatz [10] within the tight-binding approximation [11]. The observed structures of Nb_3TeCl_7, α-Nb_3Cl_8 [6], and $NbCl_4$ [12] were used, while model structures to mimic mixed crystal formation will be discussed later in the text. Energy densities of states (DOS) and crystal orbital overlap population (COOP) curves were evaluated using special ***k*** points sets [13], and tight-binding overlaps were included within two neighboring unit cells along every translational vector. Nb atomic orbital energies were corrected for charge transfer [14], and these parameters together with those for Te and Cl are listed in Table 4 [15].

Lattice energy calculations were performed using the approximation for the lattice energy as the summation of three terms [16]:

$$U_{LAT} = U_{MAD} + U_{BM} + U_{VDW} \quad (1)$$

in which U_{MAD} is the Madelung energy, U_{BM} is the Borne–Mayer repulsion energy, and U_{VDW} incorporates both dipole–dipole and dipole–quadrupole interactions, which are combined to represent the van der Waals energy. Each term is expressed as follows:

$$U_{MAD} = 14.40 \sum_{ij}{}' q_i q_j / r_{ij} \quad (2)$$

$$U_{BM} = b \sum_{ij}{}' (1 + q_i/r_i^{(0)} + q_j/r_j^{(0)}) \exp(-r_{ij}/\rho) \quad (3)$$

$$U_{VDW} = \sum_{ij}{}' c_{ij}/r_{ij}^6 + d_{ij}/r_{ij}^8 \quad (4)$$

where

$$c_{ij}\ (\text{eV Å}^6) = -1.5\alpha_i\alpha_j\epsilon_i\epsilon_j/(\epsilon_i + \epsilon_j) \quad (5)$$

$$d_{ij}\ (\text{eV Å}^8) = -0.156 c_{ij}(\alpha_i\epsilon_i/p_i + \alpha_j\epsilon_j/p_j) \quad (6)$$

Table 4 also lists the various parameters utilized in these equations. In Eqs. (2)–(4), the summations are carried out over all pairs of atoms $\{ij\}$ except when $i=j$. $r^{(0)}$ values are the so-called "basic radii" for ions as used by Bevan and Morris [17]. α represent polarizabilities, which are evaluated from the gas phase refraction indices for cations (after Pauling [1]), and estimated from experimental refraction data on crystalline salts for the anions [19]. The characteristic energies ϵ and the effective number p of outer electrons follow Mayer's recommendations [20]. Also, $\rho = 0.345$ Å. The Madelung energy U_{MAD} is evaluated using the Ewald method [21].

Table 4
Atomic parameters for lattice energy and extended Hückel calculations on Nb_3TeCl_7 (see text for brief descriptions of these variables)

Atom	q_i	$r^{(0)}$ (Å)	α (Å^3)	ϵ (eV)	p	
Nb	+3	0.80	1.80	18.78	3.00	
Te	−2	1.93	9.22	5.90	4.00	
Cl	−1	1.80	3.30	15.80	3.20	
	Orbital	H_{ii} (eV)	ζ_1	C_1	ζ_2	C_2
Nb	5s	−10.18	1.89			
	5p	−6.21	1.85			
	4d	−11.73	4.08	0.6401	1.64	0.5516
Te	5s	−20.80	2.51			
	5p	−14.80	2.16			
Cl	3s	−30.00	2.36			
	3p	−15.00	2.04			

3. Discussion

Nb_3TeCl_7 is isostructural with α-Nb_3Cl_8 [22], which may be simply described as a defect CdI_2-type structure. Therefore, the anions form an h.c.p. arrangement ($\cdots$h$\cdots \triangleq \cdots$AB$\cdots$) [23] with Nb atoms ordered in 3/8 of the octahedral holes. The pattern of cation sites generates triangular clusters in alternate layers of possible octahedral holes. Fig. 1 illustrates the cluster and its immediate anion surroundings, and Fig. 2 shows how these clusters and condensed within a single sheet to form the fundamental two-dimensional motif for this structure type.

If we assign the three Nb atoms with the single capping anion as the basic tetrahedron, from one Nb_3X_8 layer to the next, these tetrahedra are oriented antiparallel to one another (i.e. antiferroelectrically). Within the binary halides, there are two stacking variants known: (1) α-Nb_3Cl_8 [22] and (2) β-Nb_3Br_8 [24]. Ternary chalcogenide halides, Nb_3YX_7 (Y≡S, Se, Te; X≡Br, I), show three additional polymorphs, each of which adopt non-centrosymmetric space groups [25]; (3) Nb_3SeI_7 type; (4) Nb_3SBr_7 type; (5) Nb_3TeBr_7 type. Table 5 summarizes the stacking patterns of anions and the resulting space groups for these systems. Interestingly, these five different polymorphs can be separated using a structure sorting map using the anion electronegativities (after Pauling [26]), as shown in Fig. 3. Clearly,

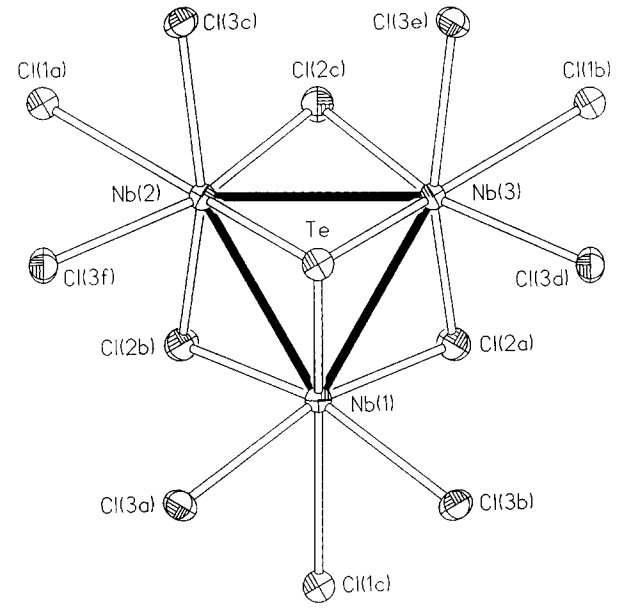

Fig. 1. The anionic environment surrounding each Nb_3 cluster (95% ellipsoids) in Nb_3TeCl_7.

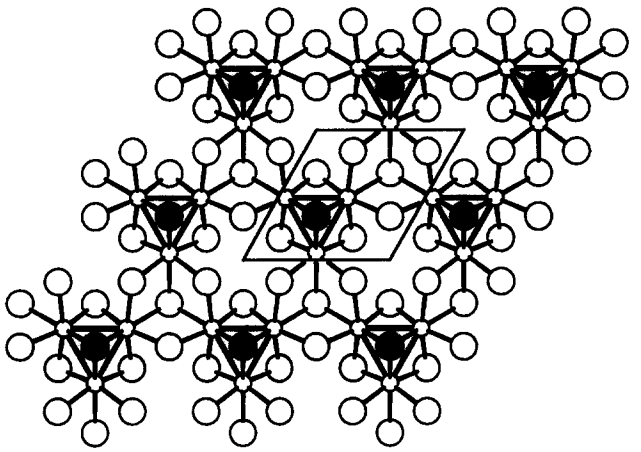

Fig. 2. (001) projection of a single layer of Nb_3TeCl_7: ○, Nb; ●, Te; ○, Cl.

Nb_3TeCl_7, which crystallizes in the space group $P\bar{3}m1$, seems anomalous on this plot.

Lattice energy calculations, however, correctly indicate the $P\bar{3}m1$ modification to be the lowest energy structure for Nb_3TeCl_7. Since there is a scale factor b in the expression for U_{BM} (see Eq. (3)), this factor was selected by assuming the lattice energy calculated for the $P\bar{3}m1$ modification to be a minimum with respect to the shortest cation–anion distance R_0 in the structure, i.e. $(\partial U_{LAT}/\partial R)|_{R=R_0}=0$. Results from these calculations are summarized in Table 5. Because of the closer proximity of chalcogenide ions in the centrosymmetric structures, the Madelung energies are generally smaller (less negative) than those for the non-centrosymmetric arrangements. However, the Born–Mayer repulsion is lowest for the observed structure ($P\bar{3}m1$). Since the calculations were performed on models in which the two-dimensional Nb_3X_8 layers were equivalent, and only their stacking modes varied, differences in U_{LAT} reflect interactions across the so-called van der Waals gaps. Thus, the stacking variant chosen by Nb_3TeCl_7 minimizes the hard core repulsions rather than minimizing the electrostatic potential. The structure sorting map in Fig. 3 suggests that the Madelung term is surprisingly more influential for the chalcogenide iodides and bromides.

How can we understand the position occupied by Te in this structure? Within each Nb_3X_8 sheet, there are four crystallographically inequivalent anion sites: (1) μ_3-X capping the triangle (μ_3-X^i); (2) μ_2-X bridging each edge of the cluster (μ_2-X^i); (3) μ_2-X bridging two clusters (μ_2-X^a); (4) μ_3-X bridging three triangles (μ_3-X^a). We can, therefore, represents these compounds as $[NbX^i_{1/3}X^i_{2/2}X^a_{2/2}X^a_{1/3}]_3$. Ternary derivatives of the binary halides, thus, offer a site preference problem. In Nb_3TeCl_7, Te replaces the μ_3-X^i halide to achieve strong Nb–Te interactions. According to relative ionic sizes in the parent Nb_3Cl_8 structure, Te would achieve optimal distances to Nb if it instead occupied the μ_3-X^a site. We performed electronic structure calculations on a two-dimensional sheet of Nb_3Cl_8 using the extended Hückel method within the tight-binding approximation. According to the rule of topological charge stabilization [27], more electronegative components will occupy sites that have greater electron densities, which, within the context of extended Hückel theory, may be estimated using a Mulliken population analysis [28]. For Nb_3Cl_8 we find the following distribution in population: μ_3-Cl^i, 6.735; μ_2-Cl^i, 6.801; μ_2-Cl^a, 7.303; μ_3-Cl^a, 7.220. Thus, the μ_3-X^i position in the Nb_3X_8 layer is the preferred site for substitution by the more electropositive chalcogens.

Fig. 4 illustrates the total DOS and the projection of Te valence orbitals for Nb_3TeCl_7. Also, the Nb–Nb COOP curve for the Nb–Nb bonds is shown. Clearly, Nb–Nb interactions are strongly bonding (calculated overlap population is 0.254), and there is a 1.5 eV gap separating occupied from unoccupied orbitals. Please note that the gap in the figure appears smaller owing to a gaussian smoothing procedure. Since extended Hückel theory, in general, overestimates band gaps because of the choice of non-orthogonal basis set, the calculated gap sets an upper bound for this system. Therefore, Nb_3TeCl_7 should be an intrinsic diamagnetic semiconductor, as is observed. The Nb–Te orbital interactions are significant to lower the Te valence orbitals by nearly 4 eV (actually, as Fig. 4 shows, Te orbitals are dispersed throughout the anion p band between -18 and -14 eV in the DOS). Since the lowest unoccupied crystal orbital also has Nb–Nb bonding character, which is similar to the results for Nb_3Br_8 [29], Nb_3TeCl_7 is an excellent candidate for intercalation by one-electron donors such as alkali metals or cob-

Table 5
Stacking variants observed for various Nb_3XY_7 compounds (results from lattice energy calculations using Nb_3TeCl_7 metrics are also listed

Structure model	Space group	Anion stacking		U_{LAT} (eV)	U_{MAD} (eV)	U_{BM} (eV)	U_{VDW} (eV)
		Type	Layers				
Nb_3TeCl_7	$P\bar{3}m1$	···h···	···AB···	120.17	137.90	28.53	10.80
Nb_3SBr_7	$P3m1$	···h···	···AB···	119.73	138.20	29.42	10.95
Nb_3TeBr_7	$P3m1$	···hc···	···ABCB···	118.34	137.55	30.10	10.89
Nb_3TeI_7	$P6_3mc$	···hc···	···ABCB···	119.86	138.37	20.41	10.91
Nb_3II_7	$R\bar{3}m1$	···hhcc···	···ABCB··· ···CABA··· ···BCAC···	118.78	137.96	29.54	10.36

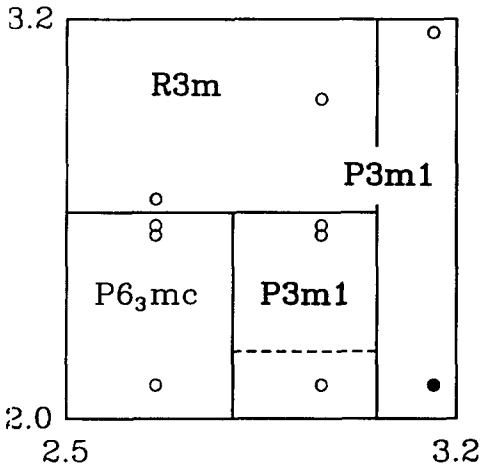

Fig. 3. Structure sorting plot for Nb_3YX_7-type compounds. ●, Nb_3TeCl_7. The scales for abscissa (X atoms) and ordinate (Y atoms) are Pauling electronegativities. Y≡S, Se, Te, Cl, Br, I; X≡Cl, Br, I. The $P3m1$ field contains two different stacking variants separated by broken line.

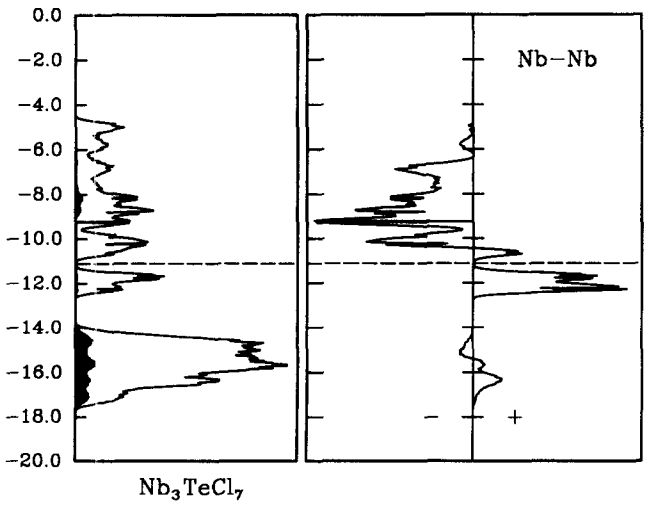

Fig. 4. Total DOS (left) and Nb–Nb COOP (right) curves for Nb_3TeCl_7. – – –, Fermi levels, The shaded portion in the total DOS is the projection of Te valence orbitals to the total DOS.

altocene [30]. However, we point out that the nature of these unoccupied orbitals is highly sensitive to the Nb–Nb distance in the cluster and loses its bonding character as the Nb–Nb distance increases towards 3.00 Å [25]. Thus, matrix effects, which are dominated by the majority anions, i.e. the halides, can greatly influence the electronic structure of these systems.

4. α-Nb_3Cl_8: electronic instabilities and homogeneity width

The success of our semiempirical calculations in rationalizing features of the new ternary Nb_3TeCl_7 prompts close examination of the electronic structure of Nb_3Cl_8 for any other phenomena. Nb_3 triangles in the solid state with six and seven valence electrons are now known [22,24,25], but more reduced clusters have yet to be completely characterized. Molybdenum oxide clusters have been structurally characterized for six through eight valence electrons [31]. Kennedy and Simon have reported intercalation of Na^+ into α-Nb_3Cl_8 [32], which strongly points towards eight-electron Nb_3 clusters, but the extent of intercalation is incomplete. Additionally, Cotton and coworkers have identified six and eight electron Nb_3 clusters in $[Nb_3Cl_{10}(PEt_3)_3]^-$ and $Nb_3Cl_7(PMe_2Ph)_6$ [33].

Numerous molecular orbital calculations have been carried out on these monocapped trimers [33,34]. Extended Hückel calculations on $Nb_3Cl_7(PMe_2Ph)_6$ as well as the $[Nb_3Cl_{13}]^{5-}$ cluster isolated from Nb_3Cl_8 give a highest occupied molecular orbital (HOMO)–lowest unoccupied molecular orbital (LUMO) gap of ca. 0.55 eV. In the two-dimensional layer Nb_3Cl_8, translational symmetry introduces the wavevectors $\boldsymbol{k}$ as an additional symmetry label and discrete orbitals are broadened into bands [28]. The intercluster orbital interactions are mediated by two sets of bridging chlorides, and for the set of levels near the Fermi level for α-Nb_3Cl_8, this overlap is extremely weak [29]. Thus, these bands are narrow and behave as localized molecular orbitals (Fig.

5). However, the gap between the highest occupied (a_1) and lowest unoccupied (e) crystal orbital is now 0.3 eV.

According to the second-order Jahn–Teller effect [35], a distortion coordinate that transforms according to the e irreducible representation ($a_1 \otimes e$) in the point group C_{3v} would couple the HOMO with the LUMO, and could drive a distortion of the cluster away from C_{3v} symmetry. Since the strength of this perturbation is inversely proportional to the HOMO–LUMO energy difference, a distortion will be more likely in the solid state than in the molecular examples. Furthermore, the Jahn–Teller theorems do not allow specification of the exact nature of this vibrational mode. Therefore, we carried out calculations that consider two different distortions of the equilateral triangle shown in Schemes 1 and 2:

1 2

(1) two short and one long Nb–Nb distance; (2) two long and one short Nb–Nb distance. These results are plotted in Fig. 5. The left-hand side of the figure indicates how condensing the $[Nb_3Cl_{13}]^{5-}$ clusters to give the two-dimensional solid shifts the energy levels near the Fermi level. To briefly describe the orbital splittings in these MO diagrams, these nine orbitals can be derived from the t_{2g} set of d orbitals as each Nb atom is nearly octahedrally coordinated by anion. When three Nb atoms interact in the equilateral triangle, the three sets of t_{2g} are split by Nb–Nb overlap to give

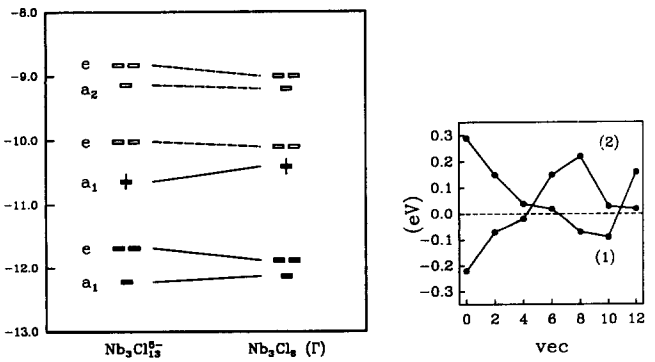

Fig. 5. the left-hand diagram shows orbital correlation for the Nb_3 cluster valence orbitals between a hypothetical isolated $[Nb_3Cl_{13}]^{5-}$ cluster and Nb_3Cl_8. The orbitals for the two-dimensional crystal are evaluated at the Γ point (0,0). The right-hand diagram shows trends in total electronic energy vs. electron count for distortion modes 1 and 2 of the Nb_3 cluster.

three Nb–Nb bonding, three essentially Nb–Nb nonbonding, and three Nb–Nb antibonding orbitals.

The right-hand side of Fig. 5 illustrates energy difference curves for the two distortion coordinates applied to the solid. Mode 1 becomes energetically preferred when the valence electron concentration rises above ca. 7.5 electrons per Nb_3 cluster. For the isolated cluster, the trends in total energy are similar, but the regular triangle remains stable for all electron counts. Thus, there is a strong effect from the HOMO–LUMO gap, which is controlled by whether the terminal ligands (chlorides in this case) are shared between clusters or not. The sensitivity of the instability to electron count is similar to the trend from trigonal planar to pyramidal geometries along the sequence BH_3, $\cdot CH_3$, NH_3 [35]. BH_3 has no Jahn–Teller active mode, but both $\cdot CH_3$ and NH_3 have an active a_{2u} mode that drives pyramidalization. Clearly, NH_3 is pyramidal, while experimental evidence suggests planar $\cdot CH_3$ but substituted pyramidal radicals. Investigations are currently underway to probe whether this structural distortion can be observed in these systems.

The other fascinating aspect of the α-Nb_3Cl_8 structure is that it occurs for a range of stoichiometries varying from $Nb_{2.56}Cl_8$ to Nb_3Cl_8 [6]. This phenomenon has been explained as mixed crystal formation between Nb_3Cl_8 and Nb_2Cl_8, which has cation pairs rather than triangles. According to the observed stoichiometries, the ratio of Nb_3 to Nb_2 clusters varies from approximately 1.2 in $Nb_{2.56}Cl_8$ to ∞ in Nb_3Cl_8. In an attempt to examine what controls the range of Cl:Nb ratios observed for these phases, we plot the total DOS for Nb_3Cl_8, $NbCl_4$, and a series of mixed trimer–dimer systems in Fig. 6 [36]. The Fermi levels for six and seven electrons per Nb_3 cluster in Nb_3Cl_8 and for two, four, and six electrons per Nb_2 cluster in $NbCl_4$ are noted. In addition, Fig. 7 illustrates the COOP curves for the two types of Nb–Nb interactions, i.e. within each Nb_3 and Nb_2 cluster, in these various structural models. In a mixed crystal, these two cluster must adopt the same chemical potential, i.e. Fermi level, and the DOS of Nb_3Cl_8 and Nb_2Cl_8 indicate that charge transfer will occur from the electron-rich, seven-electron Nb_3 clusters to the two-electron Nb_2 pairs. However, the localized nature of the orbitals in the two clusters and the large gap separating occupied from unoccupied levels in the six-electron Nb_3 cluster mean that the Nb_3 cluster will donate at most one electron to nearby dimers. Clearly, the orbitals for Nb_3 and Nb_2 cluster occur in the same energy region of the spectrum, with the three bonding levels of the Nb_3 triangle (see also Fig. 5) lying to slightly lower energies. The COOP curves nicely demonstrate how these two sets of cluster orbitals separate within the total DOS in the mixed crystals.

As the Nb_3 to Nb_2 ratio decreases, their are fewer electrons to populate Nb–Nb bonding levels in the

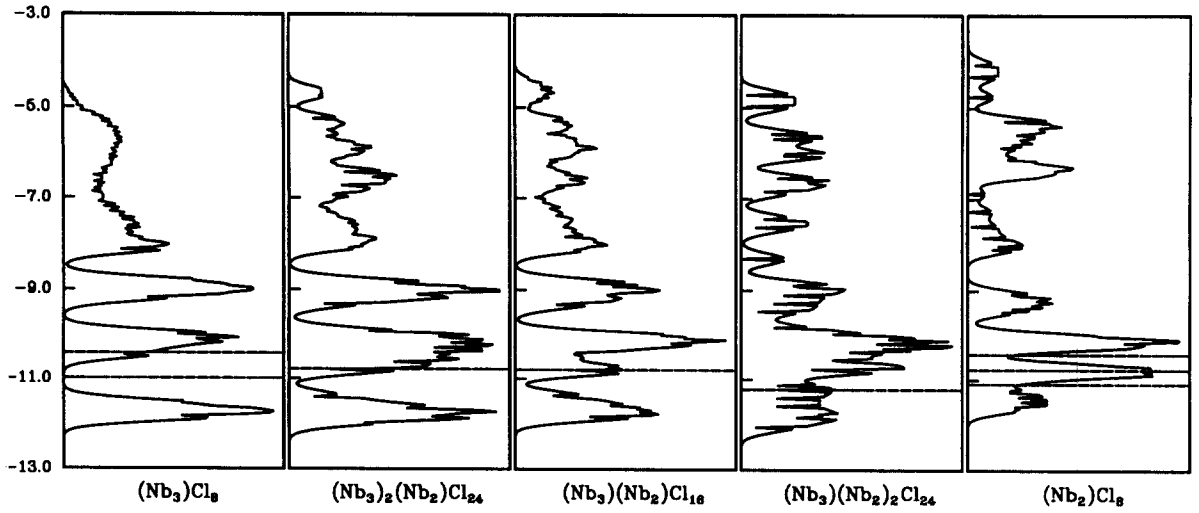

Fig. 6. Series of total DOS for various $Nb_{3-x}Cl_8$ systems. The Nb_3:Nb_2 ratio decreases from ∞ to 0 (left to right). Nb_3Cl_8: – – –, calculated Fermi levels for six and seven electrons per cluster. Nb_2Cl_8: – – –, increasing Fermi levels for two, four, and six electrons per cluster. Other $Nb_{3-x}Cl_8$ structures, – – –, Fermi level.

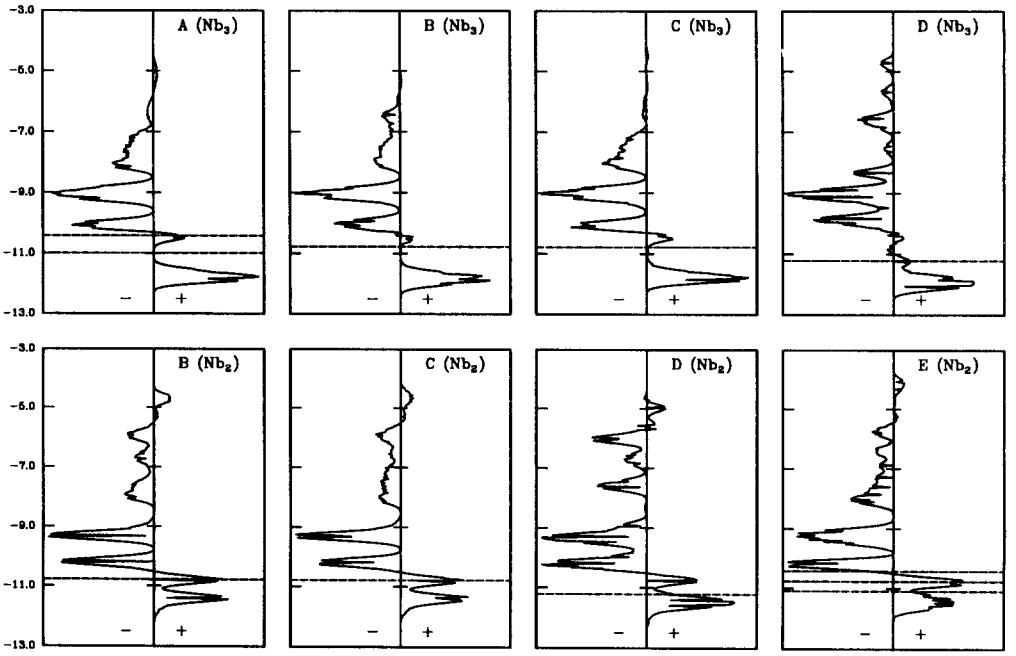

Fig. 7. Series of Nb–Nb COOP curves for various $Nb_{3-x}Cl_8$ structures: top, Nb–Nb bonds in Nb_3 clusters; bottom, Nb–Nb bonds in Nb_2 clusters. The Fermi level scheme follows Fig. 6. A, Nb_3Cl_8; B, $Nb_{2.67}Cl_8$; C, $Nb_{2.5}Cl_8$; D, $Nb_{2.33}Cl_8$; E, Nb_2Cl_8.

entire system. Below a critical electron count, which our calculations estimate to be close to $(Nb_3)(Nb_2)Cl_{16} \triangleq Nb_{2.5}Cl_8$, there is an insufficient number of electrons to occupy fully the three bonding levels of the Nb_3 cluster. At this point, the Nb–Cl system reaches a heterogeneous domain to form $Nb_{3-x}Cl_8$ and $NbCl_4$. Table 6 summarizes the electronic distribution within the Nb clusters. In the mixed systems, note how the charge of the Nb_3 clusters closely resembles the charge for the six electron cluster (2.00 electrons per Nb) when the Nb_3:Nb_2 ratio is above 1.0. However, when this ratio drops below 1.0, electrons are depleted from both clusters. Thus, we contend that there is a strong electronic driving force for the homogeneity width in the α-Nb_3Cl_8 system that stems from the relative reducing power of the seven-electron Nb_3 cluster towards

Table 6
Population analyses for the various examples in the $Nb_{3-x}Cl_8$ system (q, Mulliken populations; p, Nb–Nb overlap population)

	Nb_3:Nb_2 ratio	e^-/Nb	$q(Nb_3)$	$p(Nb_3)$	$q(Nb_2)$	$p(Nb_2)$
Nb_3Cl_8	∞	2.00	4.40	0.224	–	–
		2.33	4.66	0.248	–	–
Nb_2Cl_8	0.0	1.00	–	–	3.66	0.157
		2.00	–	–	4.51	0.205
		3.00	–	–	5.34	0.260
$Nb_{2.67}Cl_8$	2.0	2.00	4.30	0.224	4.47	0.245
$Nb_{2.50}Cl_8$	1.0	1.80	4.39	0.224	4.09	0.189
$Nb_{2.33}Cl_8$	0.5	1.57	4.15	0.210	3.67	0.168

the two-electron Nb_2 dimers. The limit on the ratio of Nb_3 to Nb_2 clusters is controlled by keeping every Nb_3 cluster at least a six-electron species.

Acknowledgements

G.J.M. thanks Professor R.A. Jacobson for the use of a Siemens P4 single-crystal diffractometer and J.E. Ostenson for magnetic susceptibility measurements. This project was supported both by the Chemical Sciences Division, Office of Basic Energy Sciences, US Department of Energy, under Contract W-7405-Eng-82 and the Donors of the Petroleum Research Fund, administered by the American Chemical Society.

References

[1] J. Rouxel, *Comments Inorg. Chem., 14* (1993) 207.
[2] J.K. Burdett and T.J. McLarnan, *Inorg. Chem., 21* (1982) 1119.
[3] S. Furuseth, L. Brattas and A. Kjekshus, *Acta Chem. Scand. A, 29* (1975) 623.
[4] J. Rijnsdorp and F. Jellinek, *J. Solid State Chem., 25* (1978) 325.
[5] J. Beck, *Angew. Chem., 106* (1994) 172; *angew. Chem., Int. Edn. Engl., 33* (1994) 163.
[6] F. Hulliger, in F. Lévy (ed.), *Structural Chemistry of Layer-Type Phases,* Reidel, Dordrecht, 1976.
[7] SHELXTL-PLUS, Version 4.0, Siemens Industrial Automation, Inc., Madison, WI.
[8] *International Tables for X-Ray Crystallography,* Vol. C, Kynoch, Birmingham, 1992.
[9] P.W. Selwood, *Magnetochemistry,* Interscience, New York, 2nd edn., 1956.
[10] R. Hoffmann and W.N. Lipscomb, *J. Chem. Phys., 36* (1962) 2179, 3489.
R. Hoffmann, *J. Chem. Phys., 39* (1963) 1397.
J.H. Ammeter, H.-B. Bürgi, J.C. Thibeault and R. Hoffmann, *J. Am. Chem. Soc., 100* (1978) 3686.
[11] M.-H. Whangbo, R. Hoffmann and R.B. Woodward, *Proc. R. Soc. London, Ser. A, 366* (1979) 23.
[12] E.A. Pisarev, D.V. Drobot and I.V. Makarchuk, *Russ. J. Inorg. Chem., Engl. Transl., 27* (1982) 10.
[13] D.J. Chadi and M.L. Cohen, *Phys. Rev. B, 8* (1973) 5747.
[14] V.I. Baranovskii and A.B. Nikolskii, *Teor. Eksp. Khim., 3* (1967) 527.
[15] E. Clementi and C. Roetti, *At. Data Nucl. Data Tables, 14* (1974) 177.
[16] F. Seitz, *The Modern Theory of Solids,* Dover Publications, New York, 1987, Chap. II.
[17] S.C. Bevan and D.F.C. Morris, *J. Chem. Soc.,* (1960) 516.
[18] L. Pauling, *Proc. R. Soc. London, Ser. A, 114* (1927) 191.
[19] S.S. Jaswal and T.P. Sharma, *J. Phys. Chem. Solids, 34* (1973) 509.
J.R. Tessman, A.H. Kahn and W. Shockley, *Phys. Rev., 92* (1953) 890.
[20] J.E. Mayer, *J. Chem. Phys., 1* (1933) 270.
[21] J.M. Ziman, *Principles of the Theory of Solids,* Cambridge University Press, London, 1964, p. 39.
[22] H.G. von Schnering, H. Wöhrle and H. Schäfer, *Naturwissenschaften, 48* (1961) 159.
[23] A.F. Wells, *Structural Inorganic Chemistry,* Oxford University Press, Oxford, 5th edn., 1984.
[24] A. Simon and H.G. von Schnering, *J. Less-Common Met., 11* (1966) 31.
[25] G.J. Miller, S. Furuseth, W. Hönle and H.G. von Schnering, to be published.
S. Furuseth, W. Hönle, G.J. Miller and H.G. von Schnering, *9th Int. Conf. on Solid Compounds of Transition Elements, Abstracts,* Royal Society of Chemistry, London, 1988.
[26] L. Pauling, *The Nature of the Chemical Bond,* Cornell University Press, Ithaca, NY, 3rd edn., 1960.
[27] J.K. Burdett, *Prog. Solid State Chem., 15* (1984) 173.
B.M. Gimarc, *J. Am. Chem. Soc., 105* (1983) 1979.
[28] R. Hoffmann, *Solids and Surfaces: A Chemist's View of Bonding in Extended Structures,* VCH, New York, 1988.
[29] H.-J. Meyer, *Z. Anorg. Allg. Chem., 620* (1994) 81.
[30] D.O'Hare, in D.W. Bruce and D. O'Hare (eds.), *Inorganic Materials, Wiley, Chichester, 1992, Chap. 4.*
[31] C.C. Toradi and R.E. McCarley, *Inorg. Chem., 24* (1985) 476.
[32] J.R. Kennedy and A. Simon, *Inorg. Chem., 30* (1991) 2564.
[33] F.A. Cotton, M.P. Diebold, X. Feng and W.J. Roth, *Inorg. Chem., 27* (1988) 3413.
[34] F.A. Cotton and T.E. Haas, *Inorg. Chem., 3* (1964) 10.
B.E. Bursten, F.A. Cotton and G.G. Stanley, *Isr. J. Chem., 19* (1980) 132.
F.A. Cotton, M.B. Hall and R. Najjar, *IInorg. Chem., 21* (1982) 302.
[35] J.K. Burdett, *Molecular Shapes, Wiley Interscience, New York, 1980.*
[37] J. Lin and G.J. Miller, *Inorg. Chem., 32* (1993) 1476.